Noncatalytic Gas-Solid Reactions and Mechanical Stress Generation

Hilmar Rode, Dariusz Orlicki, and Vladimir Hlavacek
Laboratory for Ceramic and Reaction Engineering, Dept. of Chemical Engineering,
State University of New York at Buffalo, Buffalo, NY 14260

The reaction rate in gas-solid systems can be affected by mechanical stresses that arise as the reaction proceeds. Stresses develop due to differences between precursor and product molar volumes and thermal expansion coefficients. Experimental evidence on the interaction of reaction rate and mechanical stress for the Ti/N_2 and Ti/O_2 systems is provided. A detailed and consistent mathematical model is developed for the reaction taking place at the constrained precursor/product interface. An elastic formulation for the stresses is adopted, and stress generation due to mismatches in linear thermal expansion coefficients and equivalent volume (Pilling-Bedworth ratio) for the precursor and product are considered. The effect of surface energy, which becomes significant for particle sizes below 1 μm, is also included in the model. Both experimentally and theoretically, conditions exist where the mechanical stresses exceed the strength of the material, leading to mechanical breakdown of the product layer, thus causing a discontinuity in the observed reaction rate. The entire processing history, including the reaction, temperature, and pressure profiles, plays an important role in determining the overall reaction kinetics of the powder.

Introduction

Gas-solid powder reaction systems play a fundamental role in modern industry. Typical examples where a solid product is formed, include (Kubaschewski and Hopkins, 1962; Pigford and Sliger, 1973; Szekely et al., 1976):

Roasting of sulfide ores:

$$4FeS_{2(s)} + 11O_{2(g)} \rightarrow 2Fe_2O_{3(s)} + 8SO_{2(g)}$$

Reduction of iron oxide:

$$Fe_2O_{3(s)} \xrightarrow{CO_{(g)}} Fe_3O_{4(s)} \xrightarrow{CO_{(g)}} FeO_{(s)} \xrightarrow{CO_{(g)}} Fe_{(s)}$$

SO_2 scavenging by CaO: $CaO_{(s)} + SO_{2(g)} \rightarrow CaSO_{3(s)}$
Nitridation of metallic powders: $3Si_{(s)} + 2N_{2(g)} \rightarrow Si_3N_{4(s)}$
Oxidation of metallic powders: $Ti_{(s)} + O_{2(g)} \rightarrow TiO_{2(g)}$

The gaseous reactant (also the gaseous product, if it exists) has to diffuse through the product layer. This aspect has been the focus of many studies. Several reaction models were developed to describe this type of reaction system, such as the shrinking core model (Levenspiel, 1972), the crackling core model (Park and Levenspiel, 1975), the grain model (Sohn and Szekely, 1972), the porous pellet model (Ishida and Wen, 1968), and in the field of metal oxidation, the parabolic law (Wagner, 1933) and the logarithmic law (Cabrera and Mott, 1949). In general, the precursor and product do not have the same molar volumes. Consequently, stresses develop in the solid particle as the reaction proceeds. Pilling and Bedworth (1923) first addressed this issue in the field of metal oxidation. They defined a ratio, named after them, that represents the volume of product formed compared to the volume of precursor from which it was formed. In this work we will use the Pilling-Bedworth ratio in a sense wider than metal oxidation. Selected values of Pilling-Bedworth ratios are shown in Table 1. Whenever conversion of the precursor to product takes place at the constrained precursor/product interface (Figure 1) and the Pilling-Bedworth ratio deviates from 1, growth stresses develop. While this ratio provides a qualitatively correct prediction of the occurrence of stresses, the full description is much more complicated, and even today is not fully understood.

Metallic powders have many applications, for example, as precursors for the combustion synthesis of ceramic powders

Correspondence concerning this article should be addressed to H. Rode.

Table 1. Pilling-Bedworth Ratios and Colors of Different Oxide and Nitride Phases of Ti

System	PBR	Color
TiO	1.20	Golden yellow, dark brown
Ti_3O_4	—	Black
Ti_2O_3	1.46	Dark violet
Ti_3O_5	—	Blue
TiO_2	1.73	White, red, brownish black, yellow
TiN	1.09	Gold

(Munir and Anselmi-Tamburini, 1989). High-purity ultrafine powders (Zhu et al., 1992) synthesized in plasma or flame reactors, for example, Ta, Mo, and W powders, find increasing applications in powder metallurgy. These powders are initially very reactive and adsorb significant gaseous impurities, which leads to a deterioration of their desired properties. Although the oxidation of metals has been investigated for a long time, many aspects of the process, especially regarding the generation of stresses, remain controversial, as summarized in reviews by Douglass (1969), Stringer (1970), and Taniguchi (1985). This situation holds even more so for powder materials, which exhibit many important differences if compared to macroscopic bodies. First, powders have high surface/volume ratios, and second, they have very small radii of curvature. Many investigators have addressed aspects pertaining to stress generation under conditions applicable to powders: Manning (1981) considered curvature; Romanski (1969a, 1969b) addressed the influence of surface/volume ratio and size and shape; Rozenband and Vaganova (1992) developed an ignition model for metallic powders, which takes the development of stresses into account in a simplified way.

Stresses are also important in other gas-solid reaction systems. In fact, whenever the shrinking core model with a solid product is applicable and the Pilling-Bedworth ratio is not 1, stresses will arise during the course of the reaction. Stresses can even arise when the Pilling-Bedworth ratio is close to unity due to different thermal expansion coefficients of the solid precursor and product phases. When the stresses exceed the strength of the material, the product layer will crack or undergo stress relief by some other mechanism. This point is acknowledged by the mathematical models that have been developed for the case when the product layer loses its impervious nature, for example, the crackling core model (Park and Levenspiel, 1975). Szekely et al. (1976) commented on the deleterious effects of swelling and cracking, for example, during the reduction of iron ores in furnaces. The reduction of iron oxide by carbon monoxide or hydrogen has been extensively studied (Kawasaki et al., 1962; Brill-Edwards et al., 1969). Brill-Edwards et al. (1969) found that extensive cracking occurred when hematite (Fe_2O_3) was reduced to magnetite (Fe_3O_4) due to the intrinsic volume change during the phase change. They found that disintegration of the pellets occurred purely from thermal and chemically induced stresses. Recently Pigeon and Varma (1993) took the expansion of the product layer into account during their quantitative analysis of silicon nitridation.

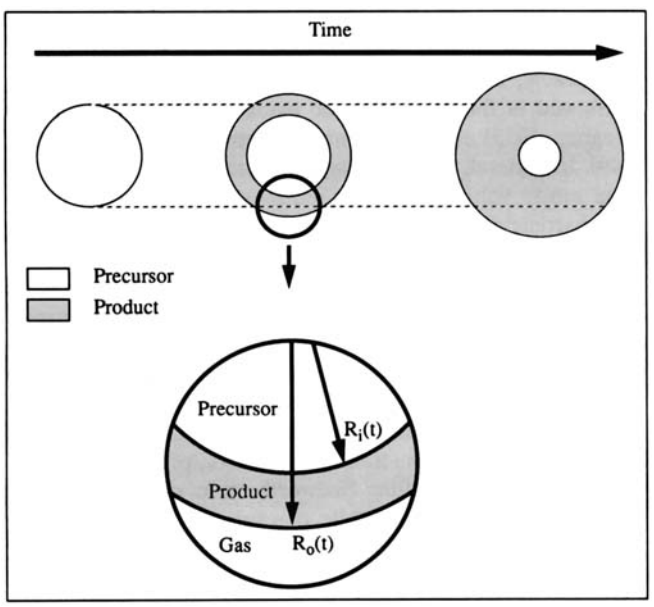

Figure 1. Reaction process showing the precursor/product and product/gas interfaces.

Thus we see that many workers have addressed the generation of stresses in gas-solid powder reaction systems in an approximate manner. However, a consistent and general model that describes the development of stresses in gas-solid powder systems and predicts when the product layer will lose its impervious nature is still lacking. Therefore, the goal of this article is to provide a consistent treatment of stress development in gas-solid reaction systems that form a nonporous solid product where the reaction takes place at the constrained precursor/product interface. We describe the process up to the point where the stresses exceed the strength of the material. Then some stress relief mechanism has to take place—it could be plastic flow, cracking and spalling of the product layer, or a variety of other mechanisms.

The article consists of two major sections. In the first part we provide experimental evidence regarding the existence of stresses in powder systems and show how they can affect powder behavior. "As received" Ti powders were aged in air to increase the initial oxygen content, and in nitrogen to increase the initial nitrogen content. The powder samples were analyzed in a simultaneous thermogravimetric–differential thermal analyzer (TGA/DTA). Further analytical procedures included oxygen/nitrogen analysis, BET surface area determination, scanning electron microscopy (SEM), X-ray diffraction (XRD), and sedimentation particle size analysis. Then a consistent mathematical formulation is developed for the description of stresses in gas-solid powder reaction systems. The model is formulated in the broadest possible terms. The thermoelastic model accounts for the generation of stresses due to the Pilling-Bedworth ratio and different thermal expansion coefficients of the precursor core and product shell. An energy balance is developed so that nonisothermal effects can be included when the equations are integrated in time. The contribution of surface energy to the resulting stress distributions is also incorporated into the model. We show how the powder can evolve depending on the entire processing *history* that it experiences. Important factors in the processing history include the ambient temperature and pressure, any temperature trends, and the reaction rate. The theoretical results

Table 2. Evolution of Ti Powder Properties

Powder	Oxygen [mass %]	Nitrogen [mass %]	Surface Area [m^2/kg]	Color
Nisso:	30 μm < d_p < 150 μm, $\bar{d}_p$ = 67 μm			
"As received"	0.07	0.00	100	Silver
"Oxidized 1"	0.48	0.01	260	Bright violet
"Oxidized 2"	1.40	0.07	400	Bluish gray
"Oxidized 3"	6.70	0.35	720	Brownish gray
"Nitrided 1"	0.15	0.69	114	
"Nitrided 2"	0.16	2.86	111	
"Nitrided 3"	0.18	6.31	116	
"Converted to TiN"	0.41	18.5	123	Gold
Micron Metals:	16 μm < d_p < 41 μm, d_p = 24 μm			
"As received"	0.12	0.00	140	Silver
"Oxidized 1"	0.46	0.02	170	Golden brown
"Oxidized 2"	1.30	0.09	200	Blue
"Oxidized 3"	2.90	0.12	260	Blue
"Nitrided 1"	0.18	0.28	170	
"Nitrided 2"	0.19	0.87	161	
"Nitrided 3"	0.20	4.58	177	
"Converted to TiN"	0.17	19.8	129	Gold

are compared to experiments performed on various Ti powders.

Experimental Evidence

Apparatus and procedure

A simultaneous TGA/DTA (model ST-736, Harrop Industries, Columbus, OH) was used to evaluate the reactivity of the Ti powders. The detailed experimental procedure has been described elsewhere (Rode and Hlavacek, 1994). Two Ti powders were tested: Ti sponge powder (Nisso), −100 mesh, 99.8% purity (Nisso powder received from Metallwerk Plansee, Reutte, Austria) and Ti sponge fines powder (Micron), −325 mesh, 99.4% purity (Micron Metals, Salt Lake City, UT). Sedimentation particle sizes were evaluated (model CAPA-700, Horiba Instruments Inc., Irvine, CA). The Nisso and Micron powders have average sedimentation particle size diameters of 67 μm and 24 μm, respectively.

The BET surface area (model 2300, Micromeritics Instruments Corp., Norcross, GA) and oxygen and nitrogen contents (model TC-436, LECO Corp., St. Joseph, MI) were also evaluated. These powder properties are shown in Table 2. SEM (model S-800, Hitachi, Gaithersburg, MD) and XRD (model Nicolet with STOE data acquisition, Philips, Mahwah, NJ) analyses were conducted on representative samples.

In order to study the effect of oxygen content, the two powders were aged in a box-type muffle furnace (Blue M Electric Co., Blue Island, IL) in an air atmosphere. Although formed in air, the developing scale was essentially an oxide, with the oxygen content 20–40 times higher than the nitrogen content (Table 2). The aging temperature was 400°C in the case of the "oxidized 1" and "oxidized 2" powders, and 520°C in the case of the "oxidized 3" powder. Aging under pure nitrogen was conducted in a tube furnace (Lindbergh, Watertown, WI) in order to study the effect of nitrogen content. The powders were aged in pure N_2 between 600 and 700°C, while the conversion to TiN experiment was conducted at 900°C. Prepurified nitrogen, minimum purity 99.998%, O_2 < 5 ppm, H_2O < 3 ppm, and extra dry oxygen, minimum purity 99.6%, H_2O < 10 ppm were used as the pure gas supplies (Cryogenic Supply, Buffalo, NY).

Results

A summary of the Nisso and Micron Ti powder properties is given in Table 2. It is interesting to consider the evolution of oxygen content, nitrogen content, and BET surface area of the powders that were aged in oxygen and nitrogen. The surface area of the Micron powder increased by a factor of about 2 during oxidation, while the Nisso powder surface area increased by a factor of 7. Both powders exhibited only modest increases in surface area when aging was conducted under nitrogen. Even after conversion to TiN, both powders remained close to their original surface areas. This phenomenon is coupled to the Pilling-Bedworth ratio for the different systems (Table 1). For oxides that form on Ti, the Pilling-Bedworth ratio is significantly larger than 1, while the Pilling-Bedworth ratio for TiN is only 1.09. Thus we anticipate that large growth stresses will develop when Ti is oxidized, which may lead to failure of the protective oxide layer and a corresponding increase in surface area.

The SEM micrographs that are shown in Figures 2 and 3 are in agreement with the surface-area measurements. Comparing the "oxidized 3" Nisso powder (Figure 2b) to the "as received" case (Figure 2a), we observe that the oxide layer cracked and in fact formed several layers. The upper part of SEM is at 400× magnification, while the bottom represents a further 5×. The cracking and spalling that took place are especially clear on the bottom enlargement. The thickness of the cracked oxide layer is approximately 2 μm. On inspection of Figures 3a and b we observe no such cracking for the Micron powder, which explains why the surface area of the Micron powder only increased by a factor of 2. Figures 2c and 3c reveal that no discernible cracking occurred in the "nitrided 3" Nisso and Micron powders even though the two powders contained similar amounts of nitrogen as the "oxidized 3" powders contained oxygen. Only after almost full conversion to TiN (Figures 2d and 3d) can we discern hairline cracks in the nitride film. These results clearly show how the development of growth stresses, which are system dependent, can affect the resulting morphology of the powder.

A protective oxide layer can change the oxidation and ignition behavior of gas-solid reaction systems such as metallic powders dramatically (Rode and Hlavacek, 1994), as shown in Figure 4 where the DTA output (a positive DTA output signifies a heat release in the sample) is plotted vs. temperature. The experiment was conducted in pure oxygen for the Micron "as received" and "oxidized 3" powders. The "as received" powder underwent a gradual transition from passivity to the ignited state at approximately 500°C. The "oxidized 3" powder, which had a relatively thick, protective oxide layer (cf. Table 2 and Figure 3b) did not undergo any oxidation until approximately 600°C, when a step change took place. At that temperature the oxide layer cracked due to growth stresses and thermal expansion coefficient mismatches. With the exposure of a fresh, unreacted Ti surface to pure oxygen

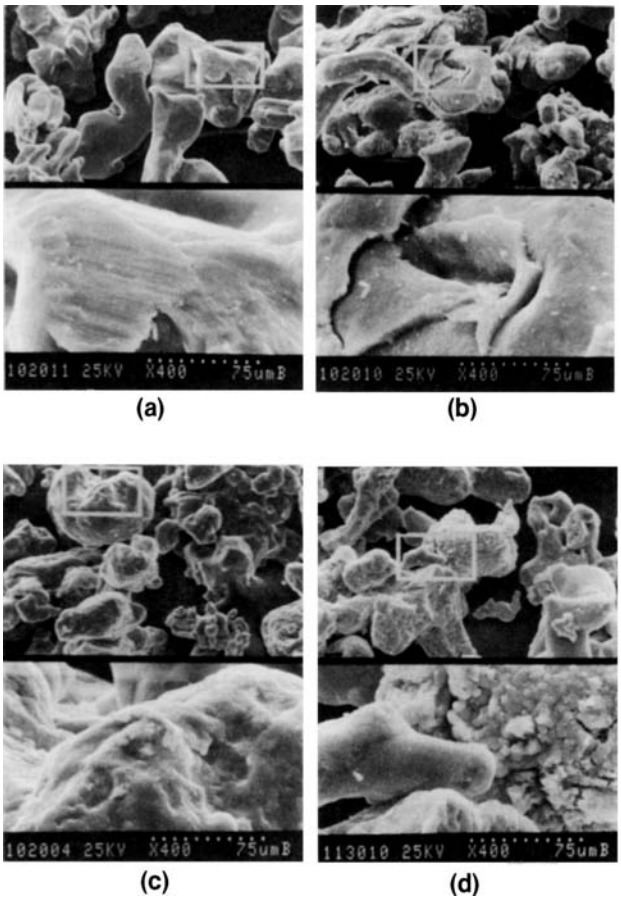

Figure 2. SEM micrographs of Nisso Ti powder at different stages of oxidation and nitridation.

(a) "As received." (b) "Oxidized 3." (c) "Nitrided 3." (d) Converted to TiN. Magnification: 400× for the upper part and further 5× for the lower.

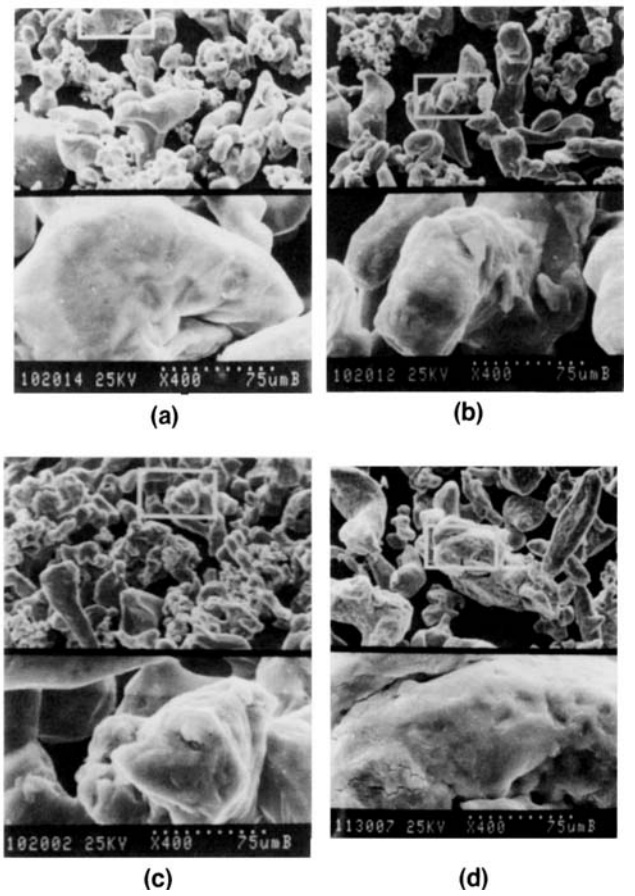

Figure 3. SEM micrographs of Micron Ti powder at different stages of oxidation and nitridation.

(a) "As received." (b) "Oxidized 3." (c) "Nitrided 3." (d) Converted to TiN. Magnification: 400× (upper) and 2,000× (lower).

at such a high temperature, ignition occurred in a step change, and the resulting exotherm was extremely large. The exotherm has been cut off for the sake of presentation, but it should be pointed out that in less than 3 s (the sampling frequency) the temperature increased from approximately 600°C to greater than the melting point of Ti (1660°C), and the sample was melted. The Ti powders that were aged in nitrogen were subjected to similar ignition tests. In all cases the ignition occurred gradually, and no sudden step-change transition to combustion was observed for the previously nitrided powders. This provides further evidence of the underlying differences between the oxygen- and nitrogen-based films on titanium.

The XRD measurements showed some interesting trends. The "as received" powders exhibited strong Ti peaks. However, the oxidized powders had much weaker Ti peaks. In the "oxidized 3" Nisso powder (but not the "oxidized 1" and "oxidized 2" powders) TiO_2 peaks were also observed. Even the "oxidized 3" Micron powder did not exhibit TiO_2 XRD peaks. The "nitrided 3" powders showed Ti_2N peaks in addi-

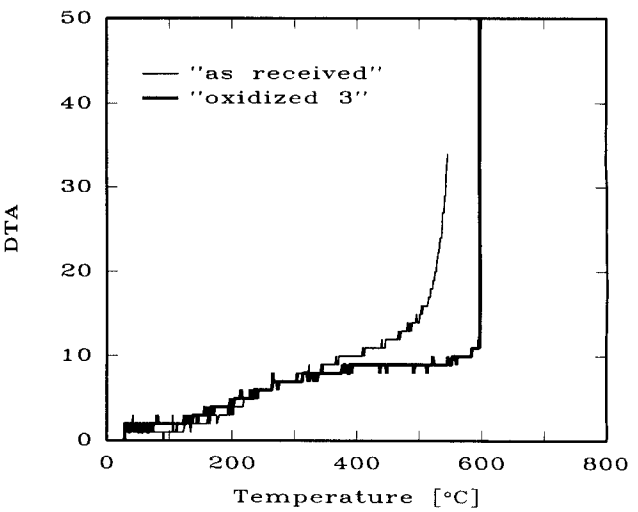

Figure 4. DTA curves of ignition behavior of "as received" and "oxidized 3" Micron Ti powder.

tion to Ti peaks, while the powders converted to TiN showed strong cubic TiN peaks.

Information regarding different titanium oxide phases can also be obtained from the colors of the oxidized powders. Data compiled by Samsanov (1973) on the colors of different titanium oxide phases are presented in Table 1. These should be compared to the colors reported in Table 2 for the oxidized Ti powders. The colors of the oxidized Ti powders were vivid, and it is likely that Ti_2O_3, Ti_3O_5, and TiO_2, and possibly also TiO, phases are present in the oxidized powders at various stages. This is important, because the lower oxide phases of Ti have lower Pilling-Bedworth ratios, which would result in lower growth stresses. It is also interesting to note that the colors exhibited by the Nisso and Micron powders were different.

Another surprising result is that the oxide film on the Micron powder was more resistant to mechanical breakdown than that on the Nisso powder. One would expect the Micron powder, which has a smaller average particle size than the Nisso powder, and thus a higher curvature, to develop larger growth stresses. This, in turn, should lead to a more rapid breakdown of the Micron oxide film. An explanation for this phenomenon rests in the purity and nature of the two powders. Tylecote (1960) conducted experiments on the oxidation of copper and nickel of different purities and found that this factor played an important part in determining the adherence of the oxide scale. He also showed that the kind of impurity (silicon and phosphorous were tested) affected the oxidation process differently.

Theoretical Analysis

A general noncatalytic gas-solid reaction system may be represented by

$$\beta_A \boldsymbol{A}_{(g)} + \beta_B \boldsymbol{B}_{(s)} \rightleftharpoons \beta_P \boldsymbol{P}_{(s)} \tag{1}$$

where a gas $\boldsymbol{A}$ and a solid precursor $\boldsymbol{B}$ react to yield a solid product $\boldsymbol{P}$. Powder particles tend to be irregular (cf. Figures 2 and 3), but in this study the idealization is made that the solid precursor powder consists of an ensemble of spherical particles. The focus of our model is on an individual particle contained within the powder bed. The location of the reaction interface is of importance. Three categories can be defined, where the first two are simple and the third represents a complex reaction mechanism:

1. The precursor is transported outward, and the reaction occurs at the product/gas interface, for example, Al/Al_2O_3 (Kubaschewski and Hopkins, 1962).
2. The oxidizing gas is transported inward, and the reaction occurs at the constrained precursor/product interface, for example, Ti/TiO_2 (Kofstad, 1962).
3. A more complex reaction mechanism occurs. The reaction can take place throughout the product layer, for example, Fe/FeO (Dunnington et al., 1952; Pfeil, 1929). Another example of a complex mechanism is the oxidation of Ta, where Pawel and coworkers (1963) reported that in addition to the oxidation of Ta to Ta_2O_5 in the product layer, significant dissolution of oxygen also occurred in the underlying precursor metal. This led to embrittlement and volume expansion, which created stresses. The work by Manning (1981) offers a suggestion for the treatment of such systems.

In this work we consider the second case, that is, the case in which reaction takes place at the constrained precursor/product interface. Several such systems exist beyond Ti/TiO_2, for example, the reduction of hematite ore (Fe_2O_3) to magnetite (Fe_3O_4) (Brill-Edwards et al., 1969) and the nitridation of silicon powder (Pigeon and Varma, 1993). Thus, the reaction takes place on the outer surface of the solid precursor core, and a shell of solid product is formed around it. The gaseous reactant penetrates the solid product layer. It should be emphasized that this gaseous reactant is completely general, and represents not only oxygen but also nitrogen, sulphur-containing gases, and halogens. Calculation of the oxidation rate is complex. Cabrera and Mott (1949), Kubaschewski and Hopkins (1962), Fromhold (1976), and Kapila and Plawsky (1993) reported ways to calculate the reaction rate during the oxidation of metals. Rode et al. (1992) calculated the oxidation rate of metallic powders employing a fundamental mechanism involving transport due to diffusion and electric field. Kinetic expressions have been developed for many other gas-solid reaction systems, for example, the reduction of iron ore by carbon monoxide (Park and Levenspiel, 1975) or the conversion of Si powder to Si_3N_4 (Pigeon and Varma, 1993). Such details are beyond the scope of the present work, and to keep the analysis general, we describe the reaction rate, $\dot{\varphi}$ (kmol/s), in general terms. The practitioner is free to choose $\dot{\varphi}$ from data provided in the literature for any given system that is applicable.

In general, the volume of solid product is different than the volume of consumed solid reactant. This phenomenon was first described by Pilling and Bedworth (1923) in the field of metal oxidation, but the concept is generally valid and will be used in a wider sense in this article. Whenever the Pilling-Bedworth ratio deviates from 1 (cf. Table 1) and the reaction takes place at the constrained precursor/product interface, growth stresses will occur. The Pilling-Bedworth ratio (PBR) can be defined as

$$PBR = \frac{\beta_P M_P}{\rho_P} \frac{\rho_B}{\beta_B M_B}. \tag{2}$$

The growing solid product that is described in Reaction 1 is modeled as a symmetric spherical shell of uniform radius r with outer and interface geometries $S_i(r)$ and $S_o(r)$, respectively, as shown schematically in Figure 1.

A detailed analysis of the time and space scales of the energy balance, presented in the Appendix, shows that an individual particle in the ensemble will be isothermal. Therefore, the temperature of the particle varies in time only due to heat exchange with its surroundings and heat generation due to the chemical reaction.

The mathematical formulation is governed by the following specific assumptions:

1. The solid substrate and the solid product are isotropic and linearly elastic materials.
2. The temperature of the system is time-dependent and can change due to heat exchange with the surroundings and the heat released by the chemical reaction.
3. Although there is no spatial variation of temperature in the system, thermostresses are present due to different thermal expansion properties of the two solids and the Pilling-Bedworth ratio.

4. The solid core and the solid product are in perfect physical contact at the precursor/product interface. The interface preserves distinguishable properties of both solids.

5. The gaseous reactant permeates the solid product, and the reaction (Eq. 1) with the solid precursor is limited to the precursor/product interface.

Mathematical formulation

Thermoelastic Stress Equations. The stress distribution associated with the growing solid film around a spherical particle due to chemical reaction is symmetrical with respect to the center. As a result of this symmetry, there are three nonzero stress components: the radial component σ_{rr}, and two angular components, $\sigma_{\theta\theta}$ and $\sigma_{\varphi\varphi}$. Since these stress components are only functions of the radial distance, r, only the equilibrium condition in the radial direction has to be taken into account (Boley and Weiner, 1960; Timoshenko and Goodier (1987)). The equilibrium equation in the radial dimension is

$$\frac{\partial \sigma_{rr}}{\partial r} + \frac{1}{r}(2\sigma_{rr} - \sigma_{\theta\theta} - \sigma_{\varphi\varphi}) = 0. \tag{3}$$

All symbols are defined in the Notation section.

The equilibrium conditions in the θ and φ directions are identically satisfied. It can be shown easily that the angular stress components $\sigma_{\theta\theta}$ and $\sigma_{\varphi\varphi}$ are identical. The stress-strain relations for isotropic materials obeying Hooke's law are

$$\epsilon_{rr} = \frac{1}{E}[\sigma_{rr} - \nu(\sigma_{\theta\theta} + \sigma_{\varphi\varphi})] + \alpha\Delta T, \tag{4}$$

$$\epsilon_{\theta\theta} = \frac{1}{E}[\sigma_{\theta\theta} - \nu(\sigma_{rr} + \sigma_{\varphi\varphi})] + \alpha\Delta T. \tag{5}$$

The strains are related to the displacements as

$$\epsilon_{rr} = \frac{\partial u}{\partial r}, \tag{6}$$

$$\epsilon_{\theta\theta} = \epsilon_{\varphi\varphi} = \frac{u}{r}. \tag{7}$$

Substituting these relations (Eqs. 4 to 7) into the equilibrium equation (Eq. 3) and assuming that there is no temperature variation in a space, the displacement formulation is obtained:

$$\frac{\partial}{\partial r}\left[\frac{1}{r^2}\frac{\partial (r^2 u)}{\partial r}\right] = 0. \tag{8}$$

The general solution of this equation is

$$u = C_1 r + \frac{C_2}{r^2}. \tag{9}$$

From the strain-displacement relations (Eqs. 6 and 7) and Hooke's law (Eqs. 4 and 5), the nonzero stress components can be written as

$$\sigma_{rr} = \frac{E}{(1-2\nu)}\frac{C_1}{3} - \frac{2E}{(1+\nu)}\frac{C_2}{r^3} - \frac{E}{(1-2\nu)}\alpha\Delta T \tag{10}$$

$$\sigma_{\theta\theta} = \frac{E}{(1-2\nu)}\frac{C_1}{3} + \frac{E}{(1+\nu)}\frac{C_2}{r^3} - \frac{E}{(1-2\nu)}\alpha\Delta T. \tag{11}$$

Reaction. The reaction represented by Eq. 1 where a gas A and a solid B yield a solid product P takes place only at the interface between the two solids (Figure 1). Since the precursor particle is in the form of a spherical particle, the reaction rate, $\dot{\varphi}$ (kmol/s), can be expressed as follows

$$\dot{\varphi}_B = -4\pi R_i^2(t)\frac{\rho_B}{M_B}\frac{dR_i(t)}{dt}. \tag{12}$$

At the same time a shell of solid product P is created around the particle so the reaction rate of Eq. 1 with respect to the solid product P can be expressed as follows, according to the stoichiometry:

$$\dot{\varphi}_P = \frac{\beta_P}{\beta_B}\dot{\varphi}_B. \tag{13}$$

Boundary Conditions. The general solution (Eqs. 9 to 11) applies to the precursor core and the product shell. The boundary conditions for the spherical precursor core and the surrounding product shell of the single particle reaction system are

1. At the center point there is no radial displacement due to symmetry:

$$u|_{r=0} = 0. \tag{14}$$

2. The outer surface is subject to compressive stresses due to external gas pressure and large positive surface curvature:

$$\sigma_{rr}|_{r=R_o(t)} = -P - \frac{2\gamma_P}{R_o(t)}. \tag{15}$$

The surface energy γ was discussed by Murray and Carey (1989). For their application this term was not important. However, for powder materials where the particle size can easily be smaller than 1 μm (Zhu et al., 1992), the curvature becomes extremely large, and the surface energy term has to be retained. The effect of surface energy on the stress distribution for surfaces with high curvature has been discussed by Kingery et al. (1976). They reported that for Al_2O_3, employing a surface energy of 0.9 J/m^2, a pressure difference of 360 atmospheres was observed over the interface for a particle diameter of 0.1 μm. Surface energies of metals are well documented (Wawra, 1976; Israelachvili, 1992; Kristyan and Olson, 1991) and generally vary between 1 and 5 J/m^2. Values for nonmetallic solids such as oxides and nitrides typically vary between 0.5 and 3 J/m^2 (Kingery et al., 1976; Barsoum and Ownby, 1981), although such data are much scarcer than for the corresponding metal. Another important factor is the effect of surface contamination on the surface energy of a compound. Kingery et al. (1976) reported that additions of oxygen or sulphur as small as 0.05% to liquid iron decreased the surface tension by 35%. They reported that the same is

Table 3. Material Parameters for Ti/TiO_2 at 300 K

Property	Value	Reference
Young Modulus [Pa]		
E_m	104×10^9	Samsonov (1968)
E_{ox}	283×10^9	Lackey et al. (1987)
Density [kg/m^3]		
ρ_m	4500	Incropera and DeWitt (1985)
ρ_{ox}	4250	Lackey et al. (1987)
Molecular weight [kg/kmol]		
M_m	47.9	Samsonov (1968)
M_{ox}	79.9	Samsonov (1973)
Thermal expansion coefficient [1/K]		
α_m	9.2×10^{-6}	Incropera and DeWitt (1985)
α_{ox}	8.0×10^{-6}	Samsonov (1973)
Poisson ratio		
ν_m	0.36	Samsonov (1968)
ν_{ox}	0.28	Lackey et al. (1987)
Surface energy [J/m^2]		
γ_m	2.6	Kristyan and Olson (1991)
γ_{ox}	2.6	Estimate
Compressive strength [Pa]		
$\sigma_{c,m}$	657×10^6	Samsonov (1968)
$\sigma_{c,ox}$	245×10^6	Samsonov (1973)
Tensile strength [Pa]		
$\sigma_{t,m}$	316×10^6	Samsonov (1968)
$\sigma_{t,ox}$	55×10^6	Samsonov (1973)
Heat capacity [J/kg/K]		
$C_{p,m}$	522	Incropera and DeWitt (1985)
$C_{p,ox}$	710	Incropera and DeWitt (1985)
Thermal conductivity [W/m/K]		
k_m	21.9	Incropera and DeWitt (1985)
k_{ox}	8.4	Incropera and DeWitt (1985)

true of the effect of oxygen on solid metal, carbide, and nitride surfaces, and that this aspect may account for discrepancies that exist in the reported literature values. In light of this discussion it was decided to use the metal surface energy for the metal as well as its corresponding nonmetal surfaces in this model. This should not introduce significant error to the results given that we are seeking qualitative agreement with the experiments. The other properties were obtained more easily from Incropera and DeWitt (1985), Samsonov (1968), and Samsonov (1973), and are shown in Table 3 for the Ti/TiO_2 system.

3. There is a discontinuity in the stress field at the interface between the solid core and the solid product due to the large surface curvature of the interface:

$$\sigma_{rr}|_{r=R_i(t)^-} = \sigma_{rr}|_{r=R_i(t)^+} - \frac{2(\gamma_B+\gamma_P)}{R_i(t)}. \tag{16}$$

4. The solid precursor and product are in perfect contact at the interface:

$$R_i(t+\Delta t) = \begin{cases} R_i(t) - \dfrac{M_B\dot{\varphi}_B}{4\pi R_i^2(t)\rho_B}\Delta t + u_{B|R_i(t+\Delta t)} \\ R_i(t) - \dfrac{M_P\beta_P\dot{\varphi}_B}{4\pi R_i^2(t)\beta_B\rho_P}\Delta t + u_{P|R_i(t+\Delta t)}. \end{cases} \tag{17}$$

Energy Balance. Consider an ensemble of unconsolidated particles brought into contact with a gas. As the reaction between a solid ***B*** and a gas ***A*** takes place, the gas deficit creates a negative pressure gradient in the bed of particles, and a flow of gas through the void space can be established. A single solid particle is subjected to energy released by chemical reaction as well as to heat exchange by interacting with other particles in the ensemble and with the surrounding gas. Inside a solid particle the heat flow is due to a conduction mechanism that requires a temperature gradient as a driving force. As explained in the Appendix, considerable temperature gradients should not occur within a solid-powder particle. The energy-balance equation for a single particle that contains an accumulation term for both solids, a source term as the reaction thermal effect on the interface, and a term for heat exchange with the surroundings, is expressed as follows:

$$\frac{\partial[(m_BC_{pB}+m_PC_{pP})T(t)]}{\partial t} = (-\Delta H)\dot{\varphi} - hS_o(t)(T(t)-T_s(t)), \tag{18}$$

where m represents the mass of solid, C_p is heat capacity, $(-\Delta H)$ stands for the heat of reaction, h is the heat transfer coefficient, and $S_o(t)=4\pi R_o^2(t)$ represents the external surface area of the particle. The mass of the two solids is stoichiometrically correlated at any point in time by

$$m_B = \frac{4}{3}\pi R_i^3(t)\rho_B, \tag{19}$$

$$m_P = \frac{4}{3}\pi(R_0^3 - R_i^3(t))\rho_B\frac{\beta_P M_P}{\beta_B M_B}, \tag{20}$$

where R_0 is initial radius of particle, $R_i(t)$ is the radius of interface, and ρ stands for density.

Estimation of the heat transfer coefficient for a single particle in an ensemble of loose particles is based on a channeling model proposed by Kunii and Suzuki (1967) for Reynolds numbers as low as 10^{-3}, and since the extremely large surface area gives rise to rapid attainment of thermal equilibrium in the system,

$$Nu = \frac{\zeta}{6(1-\epsilon)\xi}RePr, \tag{21}$$

where ζ is the particle shape factor, ϵ is the porosity of the bed, and Nu, Re, and Pr represent the Nusselt, Reynolds, and Prandtl numbers, respectively. The adjustable parameter in the model, ξ, is a measure of channel length in particle diameters.

Solution Method. The stress equilibrium equation is steady state because the stress relaxation time is much smaller than any other time scale in the process (Thiart et al., 1991). However, the overall problem is transient in nature. This time dependency is due to changes in body dimensions and accumulation of residual stresses as the reaction progresses. Additional nonlinearity is introduced since the surface energy depends on body curvature. The stress field is calculated as a superposition of stresses arising on the interface due to the

mismatch in densities of a precursor and a product of the reaction (σ'_{rr} and $\sigma'_{\theta\theta}$), and stresses created as a result of changes in surface energy and external loads (σ''_{rr} and $\sigma''_{\theta\theta}$). Since the analytical form of the stress field is known (Eqs. 10 and 11), the problem boils down to determining the constants C_1 and C_2 for the precursor core and the product layer by matching the proper boundary conditions (Eqs. 14 to 17). Satisfying the boundary condition, Eq. 14 for the precursor core requires the constant C_2 to be identically equal to zero. This simplifies the problem and limits the number of constants to be found to three.

The calculation procedure starts with a pure stressless precursor core. In the domain ($0 \le r \le R_0$) a specified number of points are set. At an initial time ($t = 0$) the system undergoes elastic deformation due to external gas pressure, and minimization of its surface energy. At the next moment in time ($t^n = t^{n-1} + \Delta t^n$) a thin shell of precursor core is consumed. According to Eq. 12, the thickness of consumed precursor shell is

$$\Delta r_B = \frac{M_B}{4\pi R^2(t)\rho_B}\dot{\varphi}_B \Delta t. \tag{22}$$

At the same time, a corresponding shell of solid product is formed around the solid core. The thickness of the reacted precursor and formed product shells are stoichiometrically related:

$$\Delta r_P = \frac{\beta_P M_P}{\rho_P}\frac{\rho_B}{\beta_B M_B}\Delta r_B, \tag{23}$$

where the ratio $((\beta_P M_P)/\rho_P)/(\rho_B/(\beta_B M_B))$ can be identified as the Pilling-Bedworth ratio.

The system is not isothermal. Information regarding temperature changes is determined by solving the energy balance. After necessary substitutions and rearrangements the energy balance equation transforms as follows:

$$\frac{4}{3}\pi\rho_B\left[C_{pB}R_i^3(t^n) + (R_0^3 - R_i^3(t^n))\frac{\beta_P M_P}{\beta_B M_B}C_{pP}\right]\frac{T^{n+1} - T^n}{\Delta t^n} - \left(M_B C_{pB} - \frac{\beta_P}{\beta_B}M_P C_{pP}\right)\dot{\varphi}_B T^n - (-\Delta H)\dot{\varphi}_B + 4\pi R_o^2(t^n)h(T^n - T_s(t^n)) = 0. \tag{24}$$

Equation 24 is a first-order differential equation that is solved using the explicit Euler time integration routine. Since the precursor and the product of the reaction show different thermal expansion behavior, changes in temperature create thermostresses that are included in our analysis.

The necessity to match the difference in volume creates elastic deformation of the precursor solid core and of the solid product shell. Since the consumption of precursor and the creation of solid product progresses due to the reaction, the incremental stress buildup takes place at every time step. The incremental stresses are computed by omitting external pressure and effects of surface energy at the interface and outer surface:

$$\Delta\sigma'_{rr}|_{r=R'_i(t+\Delta t)^-} = \Delta\sigma'_{rr}|_{r=R'_i(t+\Delta t)^+} \tag{25}$$

$$\Delta\sigma'_{rr}|_{r=R'_o(t+\Delta t)} = 0 \tag{26}$$

$$u'_B|_{R_i(t)} - \Delta r_B = u'_P|_{R_i(t)} - \Delta r_P, \tag{27}$$

and updated positions of interface and outer surface:

$$R'_i(t+\Delta t) = R_i(t) - \Delta r_B + u'_B|_{R_i(t)} \tag{28}$$

$$R'_o(t+\Delta t) = R_o(t) + u'_P|_{R_o(t)}. \tag{29}$$

Using the definition of radial displacement (Eq. 9), radial stress (Eq. 10), consumption of solid core due to the reaction (Eq. 22), creation of solid product (Eq. 23), the positions of the interface (Eq. 28) and outer (Eq. 29) surfaces, the incremental stress formulation can be expressed as follows:

$$\frac{E_B}{(1-2\nu_B)}\left(\frac{C_{1,B}}{3} - \alpha_B\Delta T\right) = \frac{E_P}{(1-2\nu_P)}\left(\frac{C_{1,P}}{3} - \alpha_P\Delta T\right) - \frac{2E_P}{(1+\nu_P)} \times \frac{C_{2,P}}{\left(R_i(t) - \dfrac{\dot{\varphi}_B M_P\beta_P\Delta t}{4\pi R_i^2(t)\rho_P\beta_B} + C_{1,P}R_i(t) + \dfrac{C_{2,P}}{R_i(t)^2}\right)^3} \tag{30}$$

$$\frac{E_P}{(1-2\nu_P)}\left(\frac{C_{1,P}}{3} - \alpha_P\Delta T\right) - \frac{2E_P}{(1+\nu_P)}\frac{C_{2,P}}{\left(R_o(t) + C_{1,P}R_o(t) + \dfrac{C_{2,P}}{R_o(t)^2}\right)^3} = 0 \tag{31}$$

$$C_{1,B}R_i(t) - \frac{\dot{\varphi}_B M_B\Delta t}{4\pi R_i^2(t)\rho_B} = C_{1,P}R_i(t) + \frac{C_{2,P}}{R_i(t)^2} - \frac{\dot{\varphi}_B M_P\beta_P\Delta t}{4\pi R_i^2(t)\rho_P\beta_B}. \tag{32}$$

This quite arduous set of nonlinear equations is solved with respect to the constants $\boldsymbol{C}$ ($C_{i,j}$ and $i = 1, 2$; $j = P, B$) using the Newton-Raphson method. Incremental stresses and displacements are calculated at every point in the domain, and the stress field and spatial coordinates of each point in the domain are updated.

Next, an additional stress field due to external pressure and surface energy in the boundary conditions (Eqs. 15 to 17) is superimposed on the solution (σ''_{rr} and $\sigma''_{\theta\theta}$). This stress field is not cumulative, unlike stress due to the growth of the oxide layer, but it is time-dependent since the boundary conditions are

$$\Delta\sigma''_{rr}|_{r=R'_i(t+\Delta t)^-} = \Delta\sigma''_{rr}|_{r=R'_i(t+\Delta t)^+} - \frac{2(\gamma_B+\gamma_P)}{R'_i(t+\Delta t)} \tag{33}$$

$$\Delta\sigma''_{rr}|_{r=R'_o(t+\Delta t)} = -P_o - \frac{2\gamma_P}{R'_o(t+\Delta t)} \tag{34}$$

$$u''_B|_{R'_i(t+\Delta t)} = u''_P|_{R'_i(t+\Delta t)} \tag{35}$$

and

$$R_o(t+\Delta t) = R'_o(t+\Delta t) + u''_P|_{R'_o(t+\Delta t)} \tag{36}$$

$$R_i(t+\Delta t) = R'_i(t+\Delta t) + u''_P|_{R'_i(t+\Delta t)}. \tag{37}$$

These equations can be rewritten in the same manner as was done in the case of the cumulative stress to obtain

$$\frac{E_B}{(1-2\nu_B)}\frac{C_{1,B}}{3} = \frac{E_P}{(1-2\nu_P)}\frac{C_{1,P}}{3} - \frac{2(\gamma_B+\gamma_P)}{R'_i(t+\Delta t)} + \frac{2E_P}{(1+\nu_P)} \times \frac{C_{2,P}}{\left(R'_i(t+\Delta t) + C_{1,P}R'_i(t+\Delta t) + \dfrac{C_{2,P}}{R'_i(t+\Delta t)^2}\right)^3} \tag{38}$$

$$\frac{E_P}{(1-2\nu_P)}\frac{C_{1,P}}{3} - \frac{2E_P}{(1+\nu_P)} \times \frac{C_{2,P}}{\left(R'_o(t+\Delta t) + C_{1,P}R'_o(t+\Delta t) + \dfrac{C_{2,P}}{R'_o(t+\Delta t)^2}\right)^3} = 0 \tag{39}$$

$$C_{1,B}R'_i(t+\Delta t) = C_{1,P}R'_i(t+\Delta t) + \frac{C_{2,P}}{R'_i(t+\Delta t)^2}. \tag{40}$$

The set of Eqs. 38 to 40 is solved iteratively, using the Newton-Raphson method.

The total stress field (σ_{rr} and $\sigma_{\theta\theta}$) found at every time step is calculated according to the following summation, which includes the additive stresses (σ'_{rr} and $\sigma'_{\theta\theta}$) created as a result of the progress of the reaction and unmatched thermal expansion coefficients, and the nonadditive stresses (σ''_{rr} and $\sigma''_{\theta\theta}$) obtained due to surface energy and external pressure:

$$\sigma_{rr}(t^n) = \sum_{i=0}^{n} \Delta\sigma'_{rr}(t^0+\Delta t_i) + \sigma''_{rr}(t^n) \tag{41}$$

$$\sigma_{\theta\theta}(t^n) = \sum_{i=0}^{n} \Delta\sigma'_{\theta\theta}(t^0+\Delta t_i) + \sigma''_{\theta\theta}(t^n). \tag{42}$$

Since the domain is time-dependent, the position of every point in space has to be updated at each time step:

$$r(t^n) = \sum_{i=0}^{n} u'(t^0+\Delta t_i) + u''(t^n). \tag{43}$$

Results

Stress results employing the detailed stress formulation are shown in this section for several representative case studies. We have used the properties of bulk oxide materials that are generally available, in contrast to properties measured specifically for product films. Existing evidence suggests, however, that the mechanical properties of growing product layers will differ from those of the corresponding bulk materials (Bradhurst and Llewelyn Leach, 1963; Hollox and Smallman, 1965). Therefore a sensitivity analysis is also conducted to establish how the stress distributions change when parameters like the

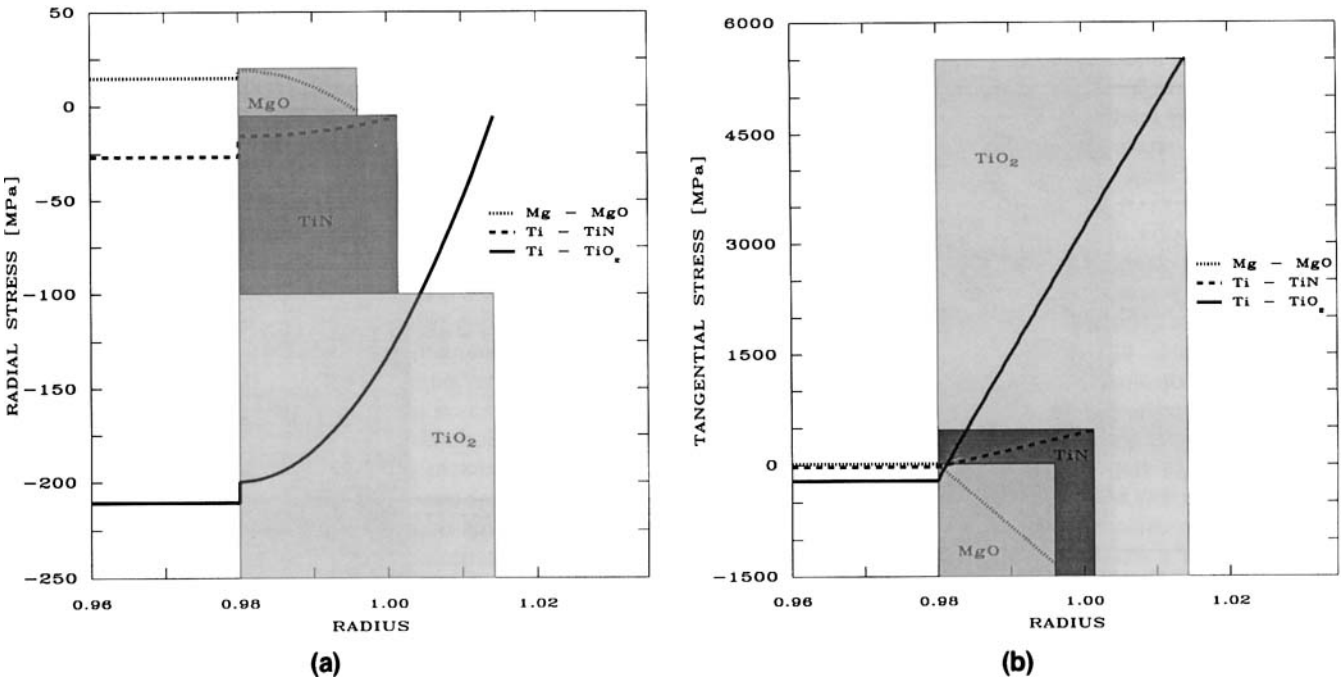

Figure 5. Stress distributions for TiO_2, TiN, and MgO for 2% conversion of the original particle radius.

(a) σ_{rr} vs. dimensionless radius, and (b) $\sigma_{\theta\theta}$ vs. dimensionless radius.

Pilling-Bedworth ratio (PBR) and the elastic modulus (E) are varied.

Stress distributions are plotted in Figure 5 for three systems with representative Pilling-Bedworth ratios: TiO_2 (PBR = 1.76), TiN (PBR = 1.09), and MgO (PBR = 0.79). The stresses are plotted against a dimensionless radius for 2% consumption of the particle by radius. Thus the reaction front is positioned at 0.98 while the outer radius has changed from 1.00 in different directions depending on the value of the PBR. In the case of TiO_2 the outer radius has increased, for TiN it has essentially remained constant, while for MgO it has actually decreased due to a PBR smaller than 1. This phenomenon is indicated by the colored boxes in Figure 5a and b. It is important to realize that the locations of both interfaces are time-dependent: the precursor/product interface due to the traveling reaction front and the product/gas interface due to the generation of growth stresses. The Ti/TiN system exhibits relatively small stresses in both the radial and tangential directions as would be expected due to the PBR, which is almost neutral (close to 1). The stresses in the Ti/TiO_2 and Mg/MgO systems differ qualitatively. In the Mg/MgO system the radial stresses are tensile, while they are compressive in the Ti/TiO_2 system. The radial and tangential stresses are constant and equal in the precurser core. Therefore the tangential stress in the Mg core is tensile, while it is compressive in the Ti core. The MgO product layer is contracted, and hence the tangential stress becomes compressive. The TiO_2 shell is expanded, and very large tensile stress is experienced in the product shell in the tangential direction. This stress substantially exceeds the tensile strength of TiO_2 (cf. Table 3), and in reality the oxide layer would have failed before an oxide layer of this thickness could be obtained. These results are consistent with the SEM micrographs shown in Figures 2 and 3 for the Ti/TiN and Ti/TiO_2 systems.

The stress evolution is shown for the Ti/TiO_2 system in Figure 6 as a function of conversion for a particle size of 1 μm. Both the radial and tangential stresses increase rapidly as the reaction front moves through the particle, and the tangential stress exceeds the tensile strength of the material by such a large factor even at relatively small conversion that mechanical failure of the product layer would certainly be observed. There is an intricate balance in place here—thicker oxide layers are chemically more resistant, which leads to a slower reaction rate as the reaction front progresses, but are under greater stress (Figure 6), which increases the probability that mechanical failure will occur. At low temperatures the oxidation of Ti typically follows the logarithmic law (Kubaschewski and Hopkins, 1962), and growth essentially stops after a product layer thickness of about 100 Å is obtained. Such a thickness is too thin for the development of stresses large enough to lead to mechanical failure. At higher temperatures, however, the reaction continues and eventually sufficiently thick product layers will result in the mechanical degradation of the film, as shown in Figure 2.

The blocks in the figures are shown to emphasize pictorially how the particle actually "swells" up due to the stress development, and in fact both interfaces represent moving boundaries. When the precursor core radius has decreased by 10%, the overall particle radius has expanded by approximately 5% as shown in Figure 6. The stresses lead to overall compression of the oxide layer when the PBR is larger than 1, and the actual volume of the oxide layer is smaller than if the layer were to grow under stress-free conditions. This effect has been reported theoretically by Murray and Carey (1989) for the case of Si oxidation in trenches for electronics applications and experimentally by Marcus and Sheng (1982).

The effect of the Pilling-Bedworth ratio on the stress distribution is shown in Figure 7. Ti can form various oxide phases in the presence of oxygen. Although TiO_2 is the most

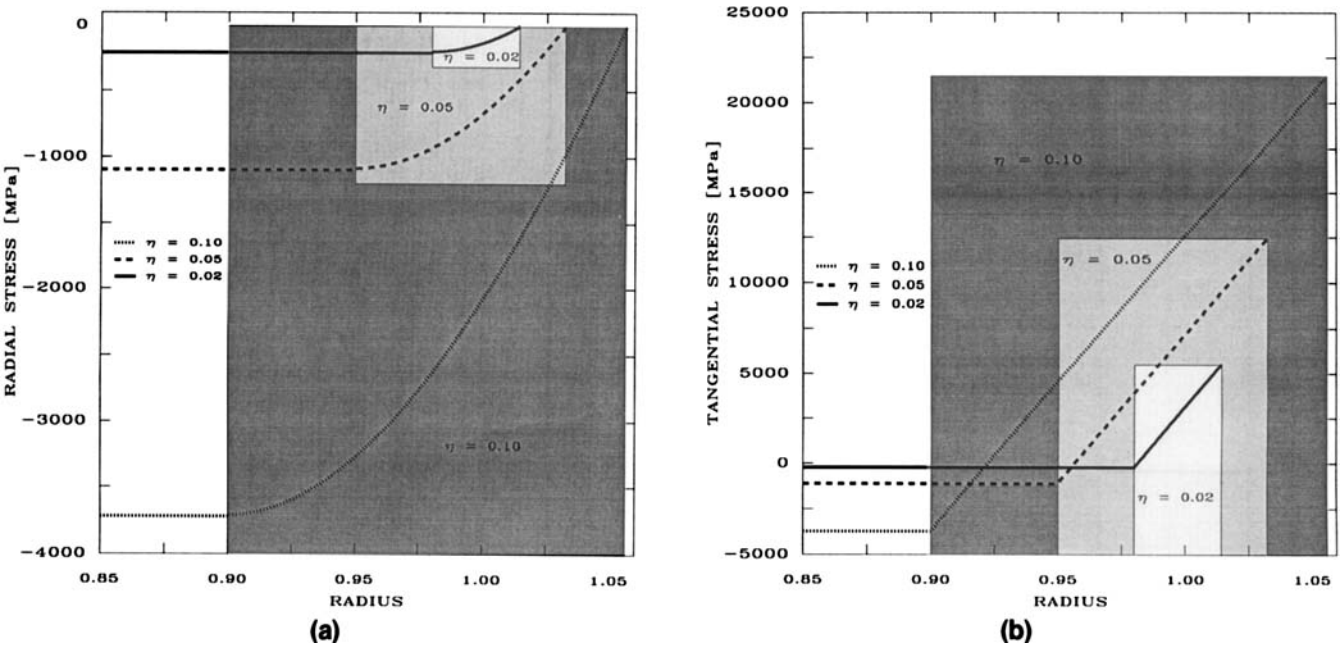

Figure 6. Stress profile vs. degree of conversion for the Ti/O_2 system.

(a) σ_{rr} vs. dimensionless radius, and (b) $\sigma_{\theta\theta}$ vs. dimensionless radius.

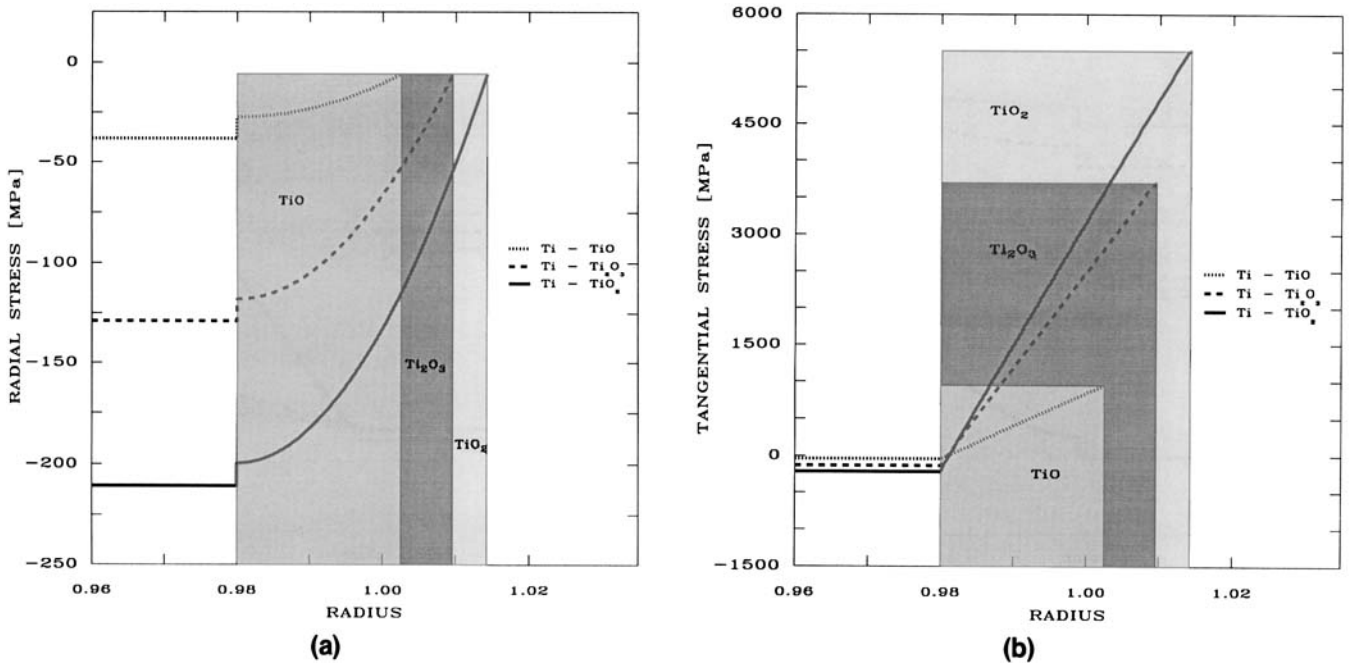

Figure 7. Effect of the Pilling-Bedworth ratio on the Ti/O_2 system for 2% conversion of the original particle radius.

(a) σ_{rr} vs. dimensionless radius, and (b) $\sigma_{\theta\theta}$ vs. dimensionless radius.

favorable phase under engineering conditions, some of the lower oxides would result in lower stresses due to smaller Pilling-Bedworth ratios (Table 1). In that sense mechanical stresses create a driving force for the formation of such lower oxide phases. Figure 7 shows that a decrease in the Pilling-Bedworth ratio due to formation of a lower oxide leads to significantly lower stresses both in the radial and tangential directions. From the magnitude of the resulting stresses it is clear that the stress distribution should also be taken into account when the formation of different phases is considered from a thermodynamical point of view. This point has been discussed by Li (1978) and by Larche and Cahn (1985), and although still somewhat controversial, is gaining acceptance. The matter is complicated even further because there is a coupling with nonstoichiometric defects—the formation of substoichiometric oxide phases—because the formation of such phases raises the yield stress of titanium dioxide (Hollox and Smallman, 1965). Hirthe and Brittain (1963) also found that the steady-state creep rate in rutile increased rapidly as the defect concentration increased, suggesting a lowering of the elastic modulus.

It is important to study the effect of the elastic modulus, E, on the resulting stress distribution for several reasons. Modulus E is strongly temperature dependent and in general decreases significantly with increasing temperatures (Samsonov, 1973). In addition, growing product layers have been known to behave very differently compared to behavior expected for a bulk material. The research on the Al/Al_2O_3 system by Bradhurst and Leach (1963) demonstrates the point well. These authors characterized the system with three types of measurements and consistently found that for alumina films the ultimate tensile strain was 3% compared to 0.07% for the bulk material (40× larger), the elastic modulus was 10× smaller than for the bulk oxide, and the ultimate strength was 5× higher than for the bulk oxide. Therefore it is likely that a value for the elastic modulus significantly smaller than the bulk oxide value may be applicable to the product layers under consideration. The effect of decreasing E is shown for the Ti/TiO_2 system in Figure 8. Decreasing E by an order of magnitude, as suggested by the experience of Bradhurst and Leach (1963), decreases the magnitude of the radial and tangential stresses approximately by an order of magnitude as well, which would lead to the formation of a much thicker product film before the occurrence of mechanical failure.

The effect of particle size on the stress distribution is shown in Figure 9 for particles of 1.0, 0.1, and 0.01 μm. Such small particle sizes have specialized applications (Zhu et al., 1992). Consider the radial stress distribution that is plotted in Figure 9a against dimensionless radius for the three particle sizes. There is a discontinuity at the precursor/product interface (radius = 0.98) due to the effect of surface energy. For the largest particle size this effect is hardly noticeable, and it is clear that the surface energy can be neglected for particle sizes above 1 μm. However, the surface energy plays a dominant role in ultrafine powders with particle sizes very much smaller than 1 μm. This fact is borne out by the differences in the profiles shown in Figure 9a and b. Without taking the contribution of surface energy into account, the three curves in each graph would have been identical. The surface energy tends to create larger compressive stresses in the radial direction and smaller tensile stresses in the tangential direction. The contribution of surface energy also creates the nonzero radial stress at the product/gas interface. This effect has been reported experimentally: Kingery et al. (1976) reported that for Al_2O_3 powder of particle size 0.1 μm a pressure difference of about 360 atmospheres was observed over the product/gas interface.

The effects of nonisothermal processing are shown in Fig-

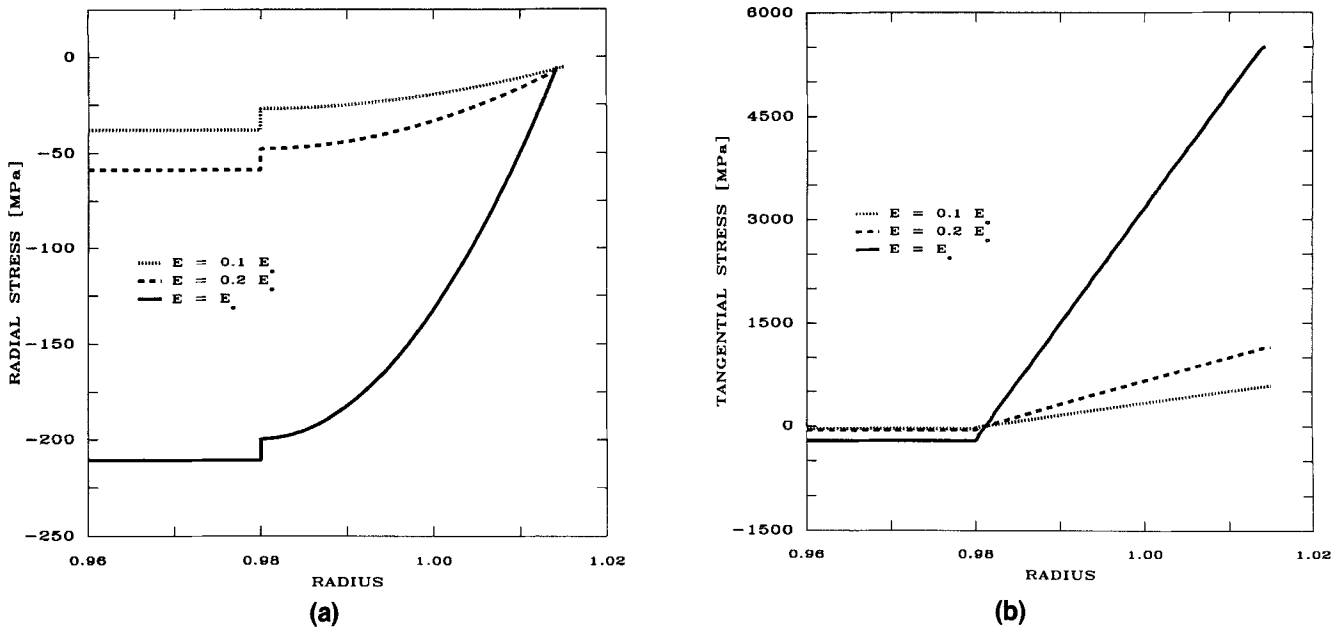

Figure 8. Effect of E on the Ti/O_2 system for 2% conversion of the original particle radius.

(a) σ_{rr} vs. dimensionless radius, and (b) $\sigma_{\theta\theta}$ vs. dimensionless radius.

ure 10 for four different cases, each corresponding to 2 mass % conversion of Ti to TiO_2 and for an initial particle size of 1 μm. In all cases the initial temperature is 298 K. In the legend for the four cases in Figure 10, T_0 is the initial temperature, T_1 is the temperature after the reaction period, and T_2 is the temperature after additional thermal treatment without further reaction. The reaction rate is constant in the period spanning T_0 to T_1. The base case, which consists of an isothermal processing history at 298 K, is represented by the solid line in Figure 10. The dashed line represents a non-isothermal reaction starting at 298 K and terminating at 600 K followed by cooling down to 298 K. The dotted line consists of an isothermal reaction at 298 K, followed by heating without further reaction to 600 K. The dotted-dashed line

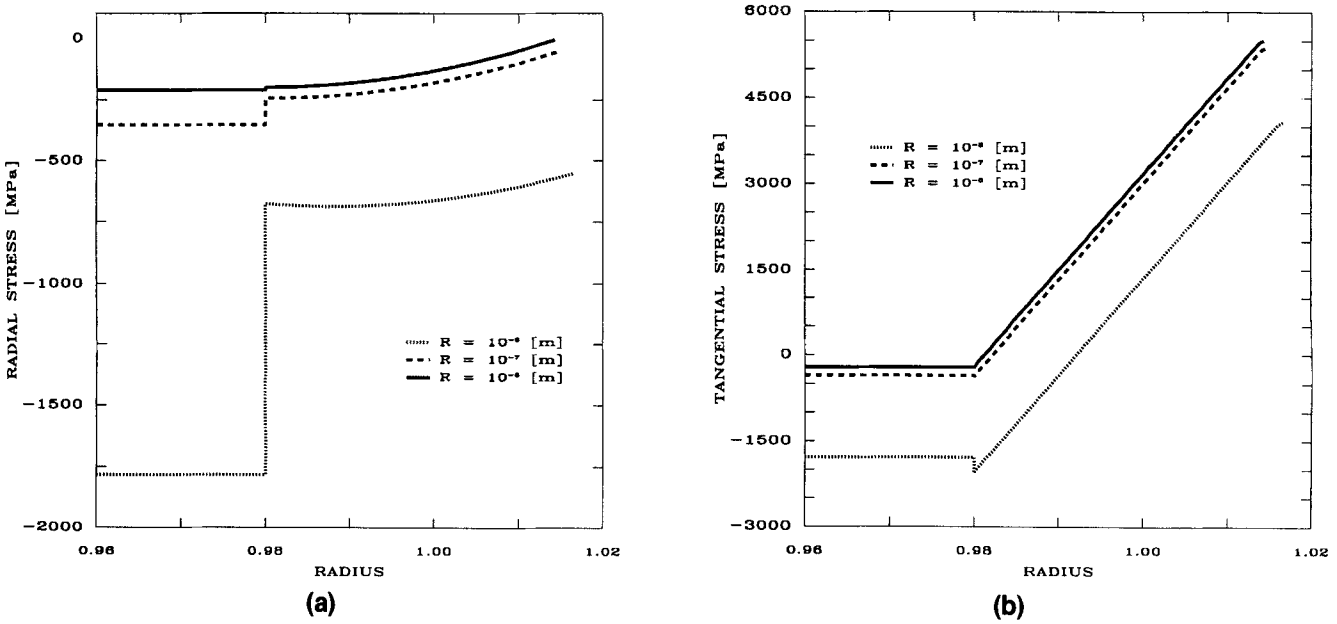

Figure 9. Influence of particle size on the stress distribution for particle sizes of 1.00, 0.10, and 0.01 μm.

(a) σ_{rr} vs. dimensionless radius, and (b) $\sigma_{\theta\theta}$ vs. dimensionless radius.

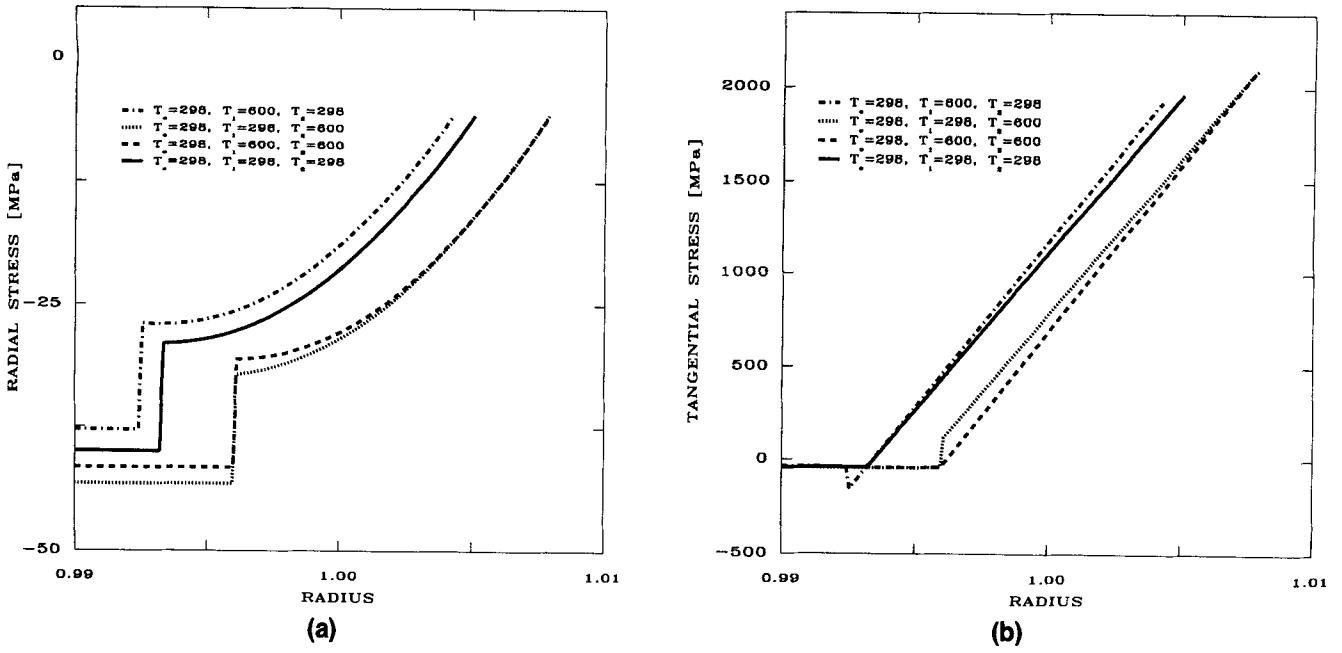

Figure 10. Influence of the temperature history on a developing stress profile.

(a) σ_{rr} vs. dimensionless radius, and (b) $\sigma_{\theta\theta}$ vs. dimensionless radius.

consists of a nonisothermal reaction up to 600 K, followed by a cool-down period to 298 K. Significant differences can be observed for the different cases in spite of the fact that the thermal expansion coefficients for the metal and oxide are very similar (9.2×10^{-6} vs. 8.0×10^{-6}, respectively). Many systems have much larger differences between the precursor and product expansion coefficients, and consequently much larger stresses would develop due to the thermal and processing history that such systems experience. Prediction of the overall behavior further depends on the ratio of the product and precursor thermal expansion coefficients—here the metal has a slightly larger coefficient than the product—often the product value would be larger and opposite trends to those shown in Figure 10 would be exhibited. As anticipated, the two cases that have final temperatures of 600 K have larger volumes than the cases with final temperatures of 300 K. Because the precursor core has a larger thermal expansion coefficient than the product shell, heating expands the core more than the product shell, leading to higher compressive stresses in the radial direction and larger tensile stresses in the tangential direction. Comparing the dotted and dotted-dashed lines, that is, those cases that experienced thermal cycling after reaction, we notice opposite trends in the tangential stress distributions at the precursor/product interfaces. In the case of the dotted-dashed line that corresponds to cooling, the precursor core would naturally contract more than the product shell for these thermal expansion coefficient values. However, there is perfect contact at the precursor/product interface, which tends to "pull" the metal core out and the product shell in. Therefore the product material at the precursor/product interface experiences a displacement that is smaller than it would be naturally, and hence there is a discontinuity in the compressive direction. The opposite argument applies to the dotted line case, which was heated up after reaction.

The results shown in Figure 10 show clearly that the processing history, especially the interaction of reaction and temperature profiles, is extremely important for such systems. Thus it is apparent that powders from different sources that have similar measurable properties such as particle size, BET surface area, oxygen content, and purity, may behave differently in ways that defy superficial explanation. A possible example is provided by McCauley et al. (1981) who attempted to correlate Zr powder burn times (PBR(Zr/ZrO_2) = 1.56, $\alpha_{Zr} = 5.9\times10^{-6}$, $\alpha_{ZrO_2} = 8.2\times10^{-6}$). These authors could not find satisfactory correlations between powders from different sources by taking the traditional physical properties into account. Another example where the thermal history of the material is of great importance, both scientifically and technologically, is in the oxidation of Si to form SiO_2 films for electronic applications as reported recently by Soleimani and Philipossian (1993). These authors reported that temperature ramping led to thermal stresses that affected the overall reaction kinetics; hence they proposed an empirical two-step oxidation theory to model the process.

In this study we assumed that the materials behave elastically. This assumption is good at low temperatures, and for dense bodies. However, plastic deformation becomes more important at higher temperatures. An interesting treatment that goes beyond the elastic formulation, is that of Murray and Carey (1989) who modeled SiO_2 as a compressible fluid with an extremely high viscosity.

In a review Douglass (1969) reported that because oxides are in general more voluminous than the underlying metals from which they are synthesized (PBR > 1), the oxide film is in compression and the metal substrate is in tension. In this

work we showed that due to the geometry encountered in powder materials the opposite trend holds, namely that the metallic core is under compression in both the radial and angular directions, while the oxide is under compression in the radial direction, but under large tension in the angular direction.

Summary and Conclusions

In this article we presented experimental evidence on the existence of mechanical stresses in noncatalytic gas-solid systems. We showed that the stresses can become very large, leading to mechanical breakdown of the product layer, thus changing the overall reaction kinetics of the solid particle in a steplike fashion.

Subsequently a consistent and general mathematical formulation was developed for the description of the stress evolution during a reaction. The model employs an elastic formulation and accounts for stresses due to volume mismatches between the precursor core and product shell as well as dissimilar thermal expansion coefficients. The contribution of surface energy to the stress profiles, important for particle sizes smaller than 1 μm, was also included.

Qualitative agreement was obtained between our mathematical formulation and the experimental evidence. The possibility of stress relief mechanisms such as plastic deformation should also be considered. In addition, a paucity of data dictated that bulk properties were used in the model. There is evidence that the properties of the growing product layer may be substantially different from bulk values, which complicates quantitative modeling.

We showed that the overall processing history, including the whole temperature, pressure, and reaction profiles that the particle experienced, can be a very important factor in giving apparently similar powders significantly different stress distributions, which could lead to vastly different behavior in terms of the overall reactivity.

In this article we developed the stress formulation in depth while simply describing the reaction rate by $\dot{\varphi}$ (kmol/s). In the next article the calculation of the reaction rate will be addressed on a fundamental level. The fundamental descriptions of transport and stress generation will then be coupled to yield a complete, consistent description of the overall particle reactivity.

Notation

d_p = sedimentation particle size (m)
k = thermal conductivity (J/m/s/K)
M = molecular weight (kg/kmol)
P = atmospheric pressure (Pa)
r = radial coordinate (m)
S = surface (m^2)
u = displacement (m)

Greek letters

α = thermal expansion coefficient (1/K)
β = stoichiometric coefficient
ϵ = strain
η = conversion
θ = angular coordinate
κ = thermal diffusivity (m^2/s)
ν = Poisson ratio
τ = time scale (s)
ϕ = angular coordinate
χ = dimensionless spatial coordinate
Ω = dimensionless temperature

Subscripts and superscripts

cond = conduction
A = gaseous reactant
B = solid precursor
i = precursor/product interface
P = solid product
ref = reference
o = product/gas interface
s = surrounding
100 = complete conversion

Literature Cited

Barsoum, M. W., and P. D. Ownby, "The Effect of Oxygen Partial Pressure on the Wetting of *SiC*, *AlN* and Si_3N_4 by *Si* and a Method for Calculating the Surface Energies Involved," in *Surfaces and Interfaces in Ceramic and Ceramic-Metal Systems*, J. Pask and A. Evans., eds., Plenum, New York, p. 457 (1981).

Boley, B. A., and J. H. Weiner, *Theory of Thermal Stresses*, Wiley, New York (1960).

Bradhurst, D. H., and J. S. Llewelyn Leach, "The Mechanical Properties of Anodic Films on Aluminium," *Trans. Br. Ceram. Soc.*, **62**, 793 (1963).

Brill-Edwards, H., H. E. N. Stone, and B. L. Daniell, "Effect of Structural Changes on the Reduction Strength of Compacted and Sintered Hematite," *J. Iron Steel Inst.*, **207**, 1565 (1969).

Cabrera, N., and N. F. Mott, "Theory of the Oxidation of Metals," *Rep. Prog. Phys.*, **12**, 163 (1949).

Douglass, D. L., "The Role of Oxide Plasticity on the Oxidation Behavior of Metals: A Review," *Oxid. Metals*, **1**, 127 (1969).

Dunnington, B. W., F. H. Beck, and M. G. Fontana, "The Mechanism of Scale Formation on Iron at High Temperature," *Corrosion*, **8**, 2 (1952).

Fromhold, A. T., *Theory of Metal Oxidation*: 1. *Fundamentals*, North-Holland, New York (1976).

Hirthe, W. M., and J. O. Brittain, "High-Temperature Steady-State Creep in Rutile," *J. Amer. Ceram. Soc.*, **46**, 411 (1963).

Hollox, G. E., and R. E. Smallman, "The Effect of Stoichiometry on the Yield Stress of *TiC* and TiO_2," *Proc. Brit. Ceram. Soc.*, **6**, 317 (1965).

Incropera, F. P., and D. P. DeWitt, *Fundamentals of Heat and Mass Transfer*, 2nd ed., Wiley, New York (1985).

Ishida, M., and C. Y. Wen, "Comparison of Kinetic and Diffusional Models for Solid-Gas Reactions," *AIChE J.*, **14**, 311 (1968).

Israelachvili, J. N., *Intermolecular and Surface Forces*, 2nd ed., Academic Press, San Diego (1992).

Kapila, D., and J. L. Plawsky, "Solid-State Film Diffusion for the Production of Integrated Optical Waveguides," *AIChE J.*, **39**, 1186 (1993).

Kawasaki, E., J. Sanscrainte, and T. J. Walsh, "Kinetics of Reduction of Iron Oxide with Carbon Monoxide and Hydrogen," *AIChE J.*, **8**, 48 (1962).

Kingery, W. D., H. K. Bowen, and D. R. Uhlmann, *Introduction to Ceramics*, 2nd ed., Wiley, New York (1976).

Kofstad, P., "Thermogravimetric Studies of the Defect Structure of Rutile (TiO_2)," *J. Phys. Chem. Solids*, **23**, 1579 (1962).

Kristyan, S., and J. A. Olson, "Statistical Mechanical Treatment of the Surface Free Enthalpy Excess of Solid Chemical Elements: 1. Temperature Dependence," *J. Phys. Chem.*, **95**, 921 (1991).

Kubaschewski, O., and B. E. Hopkins, *Oxidation of Metals and Alloys*, 2nd ed., Butterworths, London (1962).

Kunii, D., and M. Suzuki, "Particle-to-Fluid Heat and Mass Transfer in Packed Beds of Fine Particles," *Int. J. Heat Mass Transfer*, **10**, 845 (1967).

Lackey, W. J., D. P. Stinton, G. A. Cerny, A. C. Schaffhauser, and L. L. Fehrenbacher, "Ceramics Coatings for Advanced Heat Engines —A Review and Projection," *Adv. Ceram. Mat.*, **2**, 24 (1987).

Larche, F. C., and J. W. Cahn, "The Interactions of Composition and Stress in Crystalline Solids," *Acta Metall.*, **33**, 331 (1985).
Levenspiel, O., *Chemical Reaction Engineering*, 2nd ed., Wiley, New York (1972).
Li, J. C. M., "Physical Chemistry of Some Microstructural Phenomena," *Metall. Trans. A*, **9A**, 1353 (1978).
Manning, M. I., "Geometrical Effects on Oxide Scale Integrity," *Corros. Sci.*, **21**, 301 (1981).
Marcus, R. B., and T. T. Sheng, "The Oxidation of Shaped Silicon Surfaces," *J. Electrochem. Soc.*, **129**, 1278 (1982).
McCauley, J., N. D. Corbin, N. E. Rochester, J. J. DeMarco, L. Schioler, and R. Wong, "Key Physical Parameters for Predicting *Zr* Powder Burn Times," *Proc. Power Sources Symp.*, Electrochem. Soc. (1981).
Munir, Z. A., and U. Anselmi-Tamburini, "Self-Propagating Exothermic Reactions: The Synthesis of High Temperature Materials by Combustion," *Mat. Sci. Rep.*, **3**, 277 (1989).
Murray, P., and G. F. Carey, "Compressibility Effects in Modeling Thin Silicon Dioxide Film Growth," *J. Electrochem. Soc.*, **136**, 2666 (1989).
Park, J. Y., and O. Levenspiel, "The Crackling Core Model for the Reaction of Solid Particles," *Chem. Eng. Sci.*, **30**, 1207 (1975).
Pawel, R. E., J. V. Cathcart, and J. J. Campbell, "Stress Generation in Tantalum during Oxidation," *J. Electrochem. Soc.*, **110**, 551 (1963).
Pfeil, L. B., "The Oxidation of Iron and Steel at High Temperatures," *J. Iron Steel Inst.*, **119**, 501 (1929).
Pigeon, R. G., and A. Varma, "Quantitative Kinetic Analysis of Silicon Nitridation," *J. Mat. Sci.*, **28**, 2999 (1993).
Pigford, R. L., and G. Sliger, "Rate of Diffusion-Controlled Reaction Between a Gas and a Porous Solid Sphere," *Ind. Eng. Chem. Process Des. Dev.*, **12**, 85 (1973).
Pilling, N. B., and R. E. Bedworth, "The Oxidation of Metals at High Temperatures," *J. Inst. Metals*, **29**, 529 (1923).
Rode, H., V. Hlavacek, H. J. Viljoen, and J. E. Gatica, "Combustion of Metallic Powders: A Phenomenological Model for the Initiation of Combustion," *Combust. Sci. Tech.*, **88**, 153 (1992).
Rode, H., and V. Hlavacek, "An Experimental Study of Titanium Powder Reactivity in Gaseous Environments: 1. Oxidation," *Combust. Sci. Technol.*, **99**, 143 (1994).
Romanski, J., "Geometrical Factors in Studies of the Kinetics of Oxidation of Metals at High Temperatures: 1 and 2," *Corros. Sci.*, **8**, 67 (1969a).
Romanski, J., "Geometrical Factors in Studies of the Kinetics of Oxidation of Metals at High Temperatures: 3. Influence of the Shape and Size of Specimen," *Corros. Sci.*, **8**, 89 (1969b).
Rozenband, V. I., and N. I. Vaganova, "A Strength Model of Heterogeneous Ignition of Metal Particles," *Combust. Flame*, **88**, 113 (1992).
Samsonov, G. V., ed., *Handbook of Physicochemical Properties of the Elements*, Plenum, New York (1968).
Samsonov, G. V., ed., *The Oxide Handbook*, Plenum, New York (1973).
Sohn, H. T., and J. Szekely, "A Structural Model for Gas-Solid Reactions with a Moving Boundary: III. A General Dimensionless Representation of the Irreversible Reaction Between a Porous Solid and a Reactant Gas," *Chem. Eng. Sci.*, **27**, 763 (1972).
Soleimani, H. R., and A. Philipossian, "An Investigation of Two-Step Oxidation in Dry Oxygen and the Effect of Oxide Thermal History on Its Properties," *J. Electrochem. Soc.*, **140**, 1744 (1993).
Stringer, J. ,"Stress Generation and Relief in Growing Oxide Films," *Corros. Sci.*, **10**, 513 (1970).
Szekely, J., J. W. Evans, and H. Y. Sohn, *Gas-Solid Reactions*, Academic Press, New York (1976).
Taniguchi, S., "Stresses Developed during the Oxidation of Metals and Alloys," *Trans. ISIJ*, **195**, 380 (1985).
Thiart, J. J., H. J. Viljoen, K. Kriel, J. A. Puszynski, J. E. Gatica, and V. Hlavacek, "Development of Thermal Stresses in Reacting Media: 1. Failure of Catalyst Particle," *Chem. Eng. Sci.*, **46**, 351 (1991).
Timoshenko, S. P., and J. N. Goodier, *Theory of Elasticity*, 3rd ed., McGraw-Hill, New York (1987).
Tylecote, R. F., "The Adherence of Oxide Films on Metals: A Review of Information," *J. Iron Steel Inst.*, **195**, 380 (1960).
Wagner, C., "Beitrag zur Theorie des Anlaufvorgangs," *Z. Phys. Chem. B*, **21**, 25 (1933).
Wawra, H., "Zahlenvergleiche der durch Ultraschalltests oder andere konventionelle Prüfmethoden gewonnenen Werte zur Temperaturabhängigkeit der freien Oberflächenenergie fester Substanzen," *Z. Metallk.*, **66**, 395 (1976).
Zhu, C. W., G. Y. Zhao, V. V. S. Revankar, and V. Hlavacek, "Design and Development of the D.C. Plasma Reactor for the Synthesis of Ultrafine Powders," *J. Mater. Sci.*, **27**, 2211 (1992).

Appendix: Scaling Analysis for Energy Balance

In this article we deal primarily with the generation of stresses in gas-solid reaction systems, yet it is important to consider the time and space scales of the energy balance of an individual particle in an ensemble of powder particles. The heating effects associated with the reaction and heat exchange with the surroundings may be appreciable and conditions could exist where the particle is no longer isothermal. In order to check this we have to investigate the transient energy balance in the reacting particle.

Transient heat conduction in spherical coordinates (r-dependence only) with constant properties, is described by:

$$\frac{\partial T}{\partial t} = \kappa \frac{1}{r^2} \frac{\partial}{\partial r}\left(r^2 \frac{\partial T}{\partial r}\right). \tag{A1}$$

The following space scales are employed in the precursor core and product shell, respectively, to render Eq. A1 dimensionless (Figure 1):

$$\text{precursor core:} \quad \chi = \frac{r}{R_i}$$

$$\text{product shell:} \quad \chi = \frac{r - R_i}{R_o - R_i}.$$

The following conduction time scales are obtained in the two regions:

$$\text{precursor core:} \quad \tau_{\text{cond},B} = \frac{R_i^2}{\kappa_B} \tag{A2}$$

$$\text{product shell:} \quad \tau_{\text{cond},P} = \frac{(R_o - R_i)^2}{\kappa_P} \ll \frac{R_i^2}{\kappa_P}. \tag{A3}$$

Typical powder particle sizes vary between 1 and 100 μm. For this size range, relaxation of Eq. A1 occurs in the order of microseconds to milliseconds for Ti metal using $\kappa = 9.32 \times 10^{-6}$ m^2/s (Incropera and DeWitt, 1985).

Thus it is entirely reasonable to assume that conduction through the precursor core and the product shell will follow any disturbances imposed by heat generation due to chemical reaction or heat exchange with the surroundings instantaneously.

Next let us analyze any temperature gradients that will be present in the particle due to heat exchange with the surroundings (at R_o) and the heat source/sink due to chemical reaction (at R_i). The ratio of heat losses to conduction for the product layer is given by the Biot number, where it is assumed that heat losses occur by a typical convective mechanism described by a heat loss coefficient, h:

$$Bi_P = \frac{h(R_o - R_i)}{k_P} \tag{A4}$$

The ratio of heat generation due to chemical reaction to conduction for the product layer is given by the Damköhler number, where the reaction rate is specified in terms of the flux, $\dot{\varphi}$ (kmol/s):

$$Da_P = \frac{(-\Delta H)\dot{\varphi}}{T_{\text{ref}} k_P} \frac{(R_o - R_i)}{4\pi R_i^2}. \tag{A5}$$

In order to compare temperature gradients in the product shell to gradients in the precursor core, we can write:

$$\frac{(d\Omega/d\chi)_P}{(d\Omega/d\chi)_B} = \frac{k_B}{k_P} \frac{(R_o - R_i)}{R_i}. \tag{A6}$$

If the Biot and Damköhler numbers are smaller than 0.1 in both the precursor core and product shell, we can safely ignore temperature gradients and consider the entire particle to be isothermal. Each particle is contained within an ensemble of particles in a porous bed. Under these conditions (Kunii and Suzuki, 1967), and for a particle size in the range of 1 to 100 μm, the Biot number will be smaller than 0.1. Thus we can safely ignore temperature gradients in the particle due to heat losses to the surroundings.

It is more difficult to quantify the Damköhler number because the reaction rate, $\dot{\varphi}$, is often not known precisely. An estimate of the Damköhler number can be made through the following procedure, which assumes $\dot{\varphi}$ remains constant.

From Eqs. A5 and A6 the Damköhler number for the precursor core can be written as

$$Da_B = \frac{(-\Delta H)\dot{\varphi}}{T_{\text{ref}} k_B} \frac{1}{4\pi R_i}. \tag{A7}$$

Because $\dot{\varphi}$ is not known, it is difficult to evaluate Eq. A7. However, we can calculate the time required for full conversion of the precursor core to product, t_{100}, for a given Da_B. This time is

$$t_{100} = \frac{\rho_B R_i^2 (-\Delta H)}{3 M_B T_{\text{ref}} k_B} \frac{1}{Da_B}. \tag{A8}$$

For a Ti particle size of 1 μm, using the properties contained in Table 3, and $Da_B = 0.1$, t_{100} is of the order 10^{-5} s. For a 100 μm particle size, t_{100} is approximately 10^{-1} s. These values are unrealistically small (cf. Rode and Hlavacek, 1994). Thus Da_B would have to be smaller than 0.1 to obtain realistic values for t_{100}.

This means that no significant temperature gradients would result from either heat exchange to the surroundings or heat effects due to chemical reaction. Thus we can lump the temperature throughout the particle and take the particle to be isothermal. The particle temperature still remains a function of time.

Manuscript received Mar. 28, 1994, and revision received May 16, 1994.